# Comparative study of the co-assembly behaviour of 3-chloro-4-hydroxy-phenylazo dyes with DTAB†

Wenke Müller, [ID] *[a] Ralf Schweins, [ID] [a] Bernd Nöcker,[b] Joachim Kohlbrecher, [ID] [c] Glen J Smales [ID] [d] and Klaus Huber [ID] [e]

The co-assembly of three one-fold negatively charged 3-chloro-4-hydroxy-phenylazo dyes (Yellow, Blue and Red) with the cationic surfactant dodecyltrimethylammoniumbromide (DTAB) was studied to probe dye–DTAB binding stoichiometry and assembly morphology. For each dye, phase separation was observed above a given dye : DTAB ratio with the ratio depending on the dye. While Yellow and DTAB showed liquid/liquid phase separation above Yellow : DTAB = 1 : 1.67, crystalline dye–DTAB complexes were observed for Blue–DTAB and Red–DTAB above Blue : DTAB = 1 : 2.56 and Red : DTAB = 1 : 2.94 respecively. In homogeneous solution, UV/vis spectroscopic investigations suggest stochiometries of Yellow : DTAB = 1 : 2, Blue : DTAB = 1 : 3 and Red : DTAB = 1 : 4. It was concluded, that Yellow exhibits the highest dye : DTAB binding stoichiometry in both, dye–surfactant complexes in the 2-phase region and in solution, whereas the lowest dye : DTAB binding stoichiometry was observed for Red–DTAB in both cases. The observed stoichiometries are inversely correlated to the impact dye addition has on the morphology of DTAB micelles. Generally, addition of dye to DTAB micelles leads to a reduction in spontaneous curvature of these micelles and to the formation of triaxial ellipsoidal or cylindrical micelles from oblate ellipsoidal DTAB micelles. At a DTAB concentration of 30 mM and a dye concentration of 5 mM, this effect was most pronounced for Red and least pronounced for Yellow, whilst Blue showed an intermediate effect.

## Introduction

Non-covalent intermolecular interactions, leading to self- and co-assembly, are pivotal to life. They enable structures and functions ranging from cell membranes over metabolic processes to the DNA double helix. Inspired by nature, scientists are trying to exploit the spontaneous assembly of one or more components for the creation of functional materials, which could be used in regenerative medicine,[1,2] as carrier systems,[3,4] for solar cells,[5] as sensors[6,7] or in photonics.[8,9]

The complexity of intermolecular interactions exacerbates the prediction of assembly behaviour by simple models, as not only forces like van der Waals-, dipole–dipole-, electrostatic- or

π–π-interactions play a role, but other phenomena such as entropic effects, repulsive interactions, cooperativity and external forces might need to be considered.[10] This highlights the necessity of comprehensive investigations of co- and self-assembling systems to obtain a better understanding of their fundamental principles as well as the system specific features that govern assembly structures and properties.

Polyelectrolytes are a typical family of building blocks for self-assembly processes in aqueous systems, while also being a simple model system for biological building units.[11–13] One reason for this is that assembly of linear polyelectrolytes or dendrimers can be triggered by oppositely charged counter ions. To give but an example, specific counter ion binding of $Ca^{2+}$ was used to induce micellization of a block-copolyelectrolyte.[14] Morphological changes of polyelectrolyte micelles in solution can also be triggered by the addition of charged amphiphilic molecules, which is interesting for the design of well-defined nanostructures.[15] In a recent example it was shown, that the addition of ionic surfactants to an amphoteric diblock-copolyelectrolyte resulted in the formation of core–shell complexes, with an internal crystalline core structure and either positive or negative surface charge, dependent

[a] *Institut Laue-Langevin, DS/LSS, 71 Avenue des Martyrs, 38000 Grenoble, France. E-mail: we-mue@gmx.net*

[b] *KAO Germany GmbH, Pfungstädter Straße 98-100, 64297 Darmstadt, Germany*

[c] *Paul Scherrer Institut, Forschungsstrasse 111, 5232 Villigen PSI, Switzerland*

[d] *Bundesanstalt für Materialforschung und –prüfung, Unter den Eichen 87, 12205 Berlin, Germany*

[e] *Universität Paderborn, Warburger Straße 100, 33098 Paderborn, Germany*

† Electronic supplementary information (ESI) available. See DOI: https://doi.org/10.1039/d3sm00501a

on the charge of the surfactant.[16] Moreover, like the addition of inorganic counter ions or amphiphilic molecules, the introduction of charged dye molecules into polyelectrolyte systems yields supramolecular structures. These structures may be responsive to light as a trigger for morphological changes.[17] This was, among others, shown in a recent example where assembly morphology between oppositely charged polyelectrolyte and azo dye was controlled by a change in N=N-bond configuration, demonstrating the complexity of underlying intermolecular interactions.[18] Due to the interest in light-switchability, the interaction between dye molecules and polyelectrolytes has been studied for a long time, revealing that such systems form well-defined supramolecular nanoparticles of adjustable size, based on electrostatic assembly with various azo dyes.[19] Furthermore, the assembly morphology was shown to not only depend on structural features of the dye, but also on its self-assembly behaviour.[20]

The use of polymeric building blocks does, however, come along with some drawbacks. Apart from challenges arising due to availability of some polymers in sufficient purity at the needed degree of polymerization and dispersity, pathways in polymer assembly are frequently subjected to kinetic limitations.[21–23] Substituting polyelectrolytes with low molecular weight surfactants that assemble into micelles could be a pathway to circumvent such problems while obtaining assemblies with interesting and well-defined properties. To give an example, the Faul group observed the formation of highly ordered complexes between azo dye and oppositely charged surfactant molecules.[24] Some of these complexes showed pleochroism.[25] Considering the defined and regular shape of charged dye molecules and their potential to not only interact electrostatically, but also to form $\pi$–$\pi$-interactions makes them an interesting system for studying intermolecular interactions.[26]

Herein we report investigations on the stoichiometry of dye–surfactant binding between the positively charged surfactant dodecyltrimethylammoniumbromide (DTAB) and three negatively charged azo dyes (Fig. 1). The stoichiometry of dye–surfactant binding in solution is compared to the stoichiometry of dye–surfactant binding in solid complexes as obtained from the corresponding phase diagrams. Furthermore, differences in the morphology of dye–DTAB micelles were elucidated with small-angle neutron scattering (SANS).

## Experimental

### Chemicals and sample preparation

Three azo dyes Yellow (HC Yellow 16, $\geq$99%), Blue (HC Blue 18, $\geq$99.8%) and Red (HC Red 18, $\geq$99%) were provided by KAO GmbH, Germany. Completely hydrogenated dodecyltrimethylammoniumbromide (DTAB, 99%) was obtained from abcr GmbH, Germany. Completely deuterated dodecytrimethylammoniumbromide (d34-DTAB, 99% isotopic purity) was obtained from INNOVACHEM SAS, France. Tail-deuterated dodecyltrimethylammoniumbromide (d25-DTAB, 99.1% isotopic purity) was obtained from C/D/N Isotopes Inc., Canada. The buffer
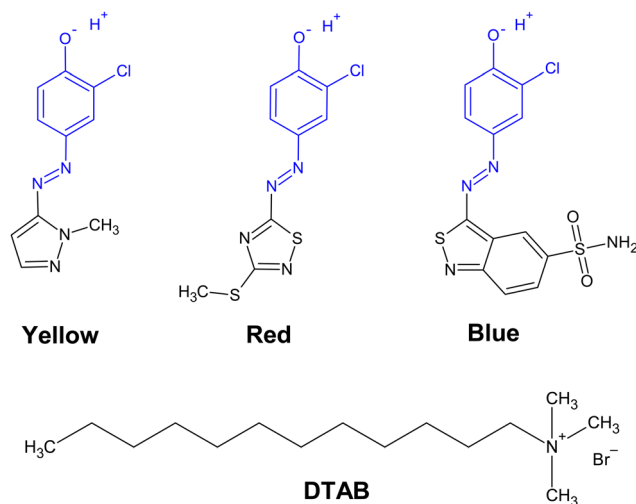


**Fig. 1** Chemical structure of three azo dyes with their common structural sub-unit marked in blue and of the cationic surfactant DTAB. At alkaline pH such as pH = 10.5, the phenolic hydroxyl group is deprotonated in all cases.

salts sodium carbonate $Na_2CO_3$ ($\geq$99.8%) and sodium bicarbonate $NaHCO_3$ ($\geq$99.7%) were obtained from Sigma Aldrich Chemie GmbH, Germany. MilliQ water was used to prepare the $NaHCO_3/Na_2CO_3$ buffer solutions (pH = 10.5, ionic strength) for UV/vis-spectroscopy and light scattering samples. $D_2O$ was used to prepare the $NaHCO_3/Na_2CO_3$ buffer solutions (pD = 10.7, ionic strength $I \approx 0.25$ M) for small-angle neutron scattering samples. $D_2O$ (99.90% D) was obtained from Eurisotop, France. Chemicals were used without further purification. Samples were prepared from stock solutions, followed by a minimum equilibration time of 20 h at room temperature prior to analysis.

### Phase diagrams

Phase diagrams were established by stepwise addition of a dye stock solution to a DTAB solution. $NaHCO_3/Na_2CO_3$ buffer solution (pH = 10.5, ionic strength $I \approx 0.25$ M) was prepared in $H_2O$ and used as a solvent in all cases. Dye stock solutions contained dye molar concentrations of 10 mM, and 15 mM for Yellow, Blue and Red respectively. The concentration of the employed DTAB stock solution was chosen according to the desired sample composition. After each addition of dye stock solution, the sample was vortexed for approximately 30 s and its visual appearance observed immediately. Phase diagrams were established at room temperature ($\approx$22 °C). Longer timescales were not systematically investigated. It should, however, be noted that at low DTAB-concentrations (below its critical micelle concentration of 9 mM) some initially stable samples showed precipitation after 24 h.

### UV/vis spectroscopy

UV/vis spectra of solutions containing dye and DTAB were recorded with a Lambda-19 spectrometer from PerkinElmer. A Hellma quartz glass cuvette with an optical path length of

0.01 cm was used. The spectrometer was equipped with a thermostat to guarantee a constant measurement temperature of 25 °C. Samples showing precipitation were filtered prior to measurement (MACHEREY-NAGEL, CHROMAFIL Xtra H-PTFE syringe filters, pore size 0.2 μm).

### Small-angle neutron scattering

Samples for small-angle neutron scattering (SANS) measurements were obtained by mixing the solvent, a dye stock solution and a stock solution containing DTAB at appropriate ratios. The solvent was a $NaHCO_3/Na_2CO_3$ buffer in $D_2O$ (pD = 10.7, ionic strength $I \approx 0.25$ M). The sample containing [Blue] = 5 mM and [DTAB] = 30 mM represents an exception to this procedure, as it was initially prepared for another project. For this sample, the solvent, a dye stock solution and a stock solution containing $d^{25}$-DTAB and $d^{34}$-DTAB at a ratio of 46 : 54 (v/v) were mixed at appropriate ratios. The solvent was a $NaHCO_3/Na_2CO_3$ buffer prepared in a mixture of $H_2O : D_2O = 50 : 50$ (v/v) (pH/D = 10.5, ionic strength $I \approx 0.25$ M). The resulting SANS curve of this sample and its fit were scaled by a factor of 3.6 in Fig. 5 to account for the difference in contrast.

After their preparation, sample solutions were filtered (MACHEREY-NAGEL, CHROMAFIL Xtra H-PTFE syringe filters, pore size 0.2 μm) into a dust-free sample vial and equilibrated for a minimum of 20 h at room temperature.

SANS measurements were performed at the instrument D11 at the Institut Laue-Langevin (ILL, Grenoble, France) and at the instrument SANS-I at the Paul Scherrer Institute (PSI, Villigen, Switzerland).

At the ILL, different setups were used: (1) the sample containing no dye and $[DTAB]_{tot} = 30$ mM and the sample containing $[Blue]_{tot} = 5$ mM and $[DTAB]_{tot} = 30$ mM were measured at three sample-to-detector distances (28 m collimation 28 m), (8 m collimation 8 m), (1.7 m collimation 4.0 m) at a neutron wavelength of 6 Å to cover a $q$-range of 0.002 Å$^{-1}$ to 0.5 Å$^{-1}$. A circular neutron beam with a diameter of 15 mm was used. (2) All samples containing Red were measured at three sample-to-detector distances (38.0 m collimation 40.5 m), (10.5 m collimation 10.5 m), (2.5 m collimation 2.5 m) at a neutron wavelength of 6 Å to cover a $q$-range of 0.0014 Å$^{-1}$ to 0.5 Å$^{-1}$. A circular neutron beam with a diameter of 14 mm was used. Neutrons were detected with a $^3$He-detector (Reuter-Stokes multi-tube detector consisting of 256 tubes with a tube diameter of 8 mm and a pixel size of 8 mm × 4 mm), detector images azimuthally averaged, corrected to the transmission of the direct beam and scaled to absolute intensity using the Mantid software.[27,28] Solvent scattering and empty cell scattering were subtracted from the scattering curves.[29] SANS data were collected at a sample temperature of 25 °C.

The sample containing $[Blue]_{tot} = 5$ mM and $[DTAB]_{tot} = 20$ mM and all samples containing Yellow were measured at the PSI SANS-I instrument. The measurements were performed at 3 sample-to-detector distances (18.0 m collimation 18.0 m), (6.0 m collimation 6.0 m), (1.6 m collimation 6.0 m) at a wavelength of 6 Å to cover a $q$-range of 0.003 Å$^{-1}$ to 0.4 Å$^{-1}$. A circular neutron beam with a diameter of 14 mm was used.

Neutrons were detected with a 2D MWPC CERCA $^3$He-detector with 128 × 128 elements of 7.5 × 7.5 mm$^2$. Detector images were corrected for pixel efficiency using scattering from a water sample which also served as a secondary standard, corrected for transmission and azimuthally averaged using the BerSANS software.[30] Solvent scattering and empty cell scattering were subtracted from the scattering curves.[29] SANS data were collected at a sample temperature of 25 °C.

Data analysis was performed with the SasView small angle scattering analysis software. In all cases, the solvent scattering length density was fixed to the known value and the assembly volume fraction was calculated based on known sample composition and partial molar volumes of each component, assuming that all molecules take part in assembly formation. This yielded an estimation of the assembly volume fraction, which was fixed to the calculated value during fitting to avoid over parameterization. The scattering length density (SLD) of the assembly was fitted. Molar volumes and complete parameter sets can be found in the ESI.†

## Discussion

### Phase diagrams

Adding dye to a solution of the cationic surfactant DTAB leads to a concentration-dependency of solution stability. This is visualized by phase diagrams shown in Fig. 2. In all cases, a homogeneous solution was obtained for sufficient surfactant excess and denoted as 1-phase region in each phase diagram. Phase separation and concomitant entry into a 2-phase region was observed at different dye : DTAB ratios for each dye and will be discussed in the following. Within the selected concentration region, the correlation between the dye concentration $[Dye]_{tot}$ and DTAB concentration $[DTAB]_{tot}$ where phase separation occurs can be described by a linear relationship (eqn (1)).

$$[Dye]_{tot} = A \cdot [DTAB]_{tot} + B \tag{1}$$

In case of Yellow and DTAB a liquid/liquid phase separation is observed. Combining either Blue or Red with the cationic surfactant DTAB gives rise to the formation of solid complexes above a threshold ratio of dye and DTAB concentration. The formation of such solid dye–surfactant complexes, from oppositely charged species, was described previously for various systems.[24,25,31,32]

Determining the phase transition threshold line according to eqn (1) indicates the stoichiometry of dye–surfactant complex formation within the observed concentration range (2 mM $\leq [DTAB]_{tot} \leq 30$ mM). This was done by a linear fit to the compositions of samples containing the highest concentration of dye still being within the 1-phase region. Data points used for fitting are highlighted in the corresponding phase diagrams.

For Yellow and DTAB, $A = 0.60$ and $B = 1.29$ mM suggests a stoichiometry of $[Yellow]_{tot} : [DTAB]_{tot} = 1:1.67$ for an entry into the 2-phase region. At low DTAB concentration, a deviation
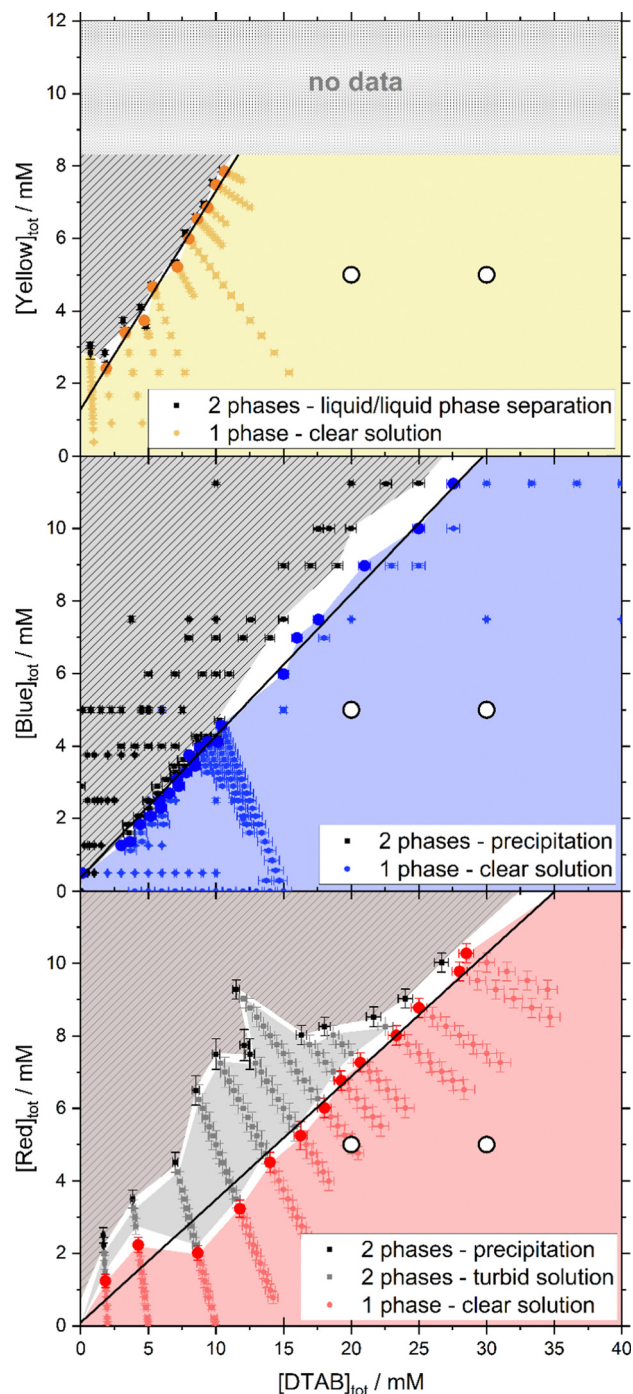
Fig. 2 Concentration-dependent phase behaviour and linear fit of phase transition threshold line (eqn (1)) for Yellow ($A$ = 0.60, $B$ = 1.29 mM), Blue ($A$ = 0.39, $B$ = 0.38 mM) and Red ($A$ = 0.34, $B$ = 0.09 mM) in combination with DTAB. The phase transition threshold line was obtained from fitting to the sample compositions marked with bold points in the 1-phase region. All phase diagrams were observed 30 s after mixing and at room temperature. The solvent was an aqueous $NaHCO_3/Na_2CO_3$-buffer in all cases. In the Yellow/DTAB diagram, dye concentrations higher than 8 mM were not accessible, as the Yellow stock solution used for sample preparation would have exceeded the solubility limit of Yellow. White circles (○) display the composition of samples which were investigated with SANS.

from this linearity was observed and not included into the linear fit. This is not unexpected, as the 1-phase region should extend to $[Yellow]_{tot}$ = 11 mM, *i.e.* the solubility limit of Yellow in the absence of DTAB.[33] As Blue and Red show a very high solubility (>25 mM) in the present buffer system and the absence of DTAB, a similar deviation at low DTAB concentration is expected for both of them.[33] It was, however, not observed in the investigated DTAB concentration range and likely happens at even lower DTAB concentrations.

The phase diagram of Blue and DTAB shows a defined phase transition. In the 2-phase region precipitates with crystalline appearance are formed. This suggests high ordering of the complexes, which was confirmed by wide-angle X-ray scattering (WAXS) measurements shown in the ESI† (Fig. S3). From a linear fit based on eqn (1) a stoichiometry of $[Blue]_{tot}:[DTAB]_{tot}$ = 1:2.56 was determined.

The phase transition threshold between the 1- and 2-phase region is less defined for Red and DTAB. Within the reported observation time of 30 s, two different 2-phase-regions were observed, one appearing as a turbid solution, likely due to liquid/liquid phase separation, and the other one showing unambiguous precipitation of crystalline Red–DTAB-complexes. A linear fit based on eqn (1) was performed to obtain information on the transition from the 1-phase-region into the 2-phase-region, independent of the appearance of the 2-phase-region. It yielded a stoichiometry for Red–DTAB complex formation of $[Red]_{tot}:[DTAB]_{tot}$ = 1:2.94. It should be noted that not all samples containing dye and DTAB in the 1-phase-region were long-term stable. Some samples close to the precipitation threshold were stable within the observation time of 30 s, but precipitated after 1 h to 1 day. This occurred more frequently at $[DTAB]_{tot}$ below the critical micelle concentration of DTAB.

To conclude this section, the excess of DTAB molecules needed to enter the soluble 1-phase-region differs for all three dyes and increases from 1.67 for Yellow over 2.56 for Blue to 2.94 for Red. The formation of dye–surfactant complexes with a defined stoichiometry is observed in most of the investigated DTAB concentration range.

## UV/vis-spectroscopy

Dye–surfactant aggregation is commonly studied by means of UV/vis-spectroscopy and various models were developed to quantitatively evaluate dye–surfactant interaction.[32,34–37] These models rely on a change in dye absorption upon addition of surfactant, which is explained by the interaction between dye and surfactant causing a polarity change in the microenvironment of the dye.[34,38] For the dyes Yellow, Blue and Red a bathochromic shift of their absorption maximum and an increase in its extinction upon successive addition of DTAB in the 1-phase region was observed (Fig. 3). It should be pointed out, that for a given dye concentration the 1-phase region only exists at sufficiently high DTAB concentrations (Fig. 2). At low DTAB concentrations, the 2-phase region occurs due to liquid/liquid phase separation or precipitation of dye–DTAB complexes. Therefore, Fig. 3 only shows absorption spectra of dye–DTAB solutions in the 1-phase region in comparison to the absorption
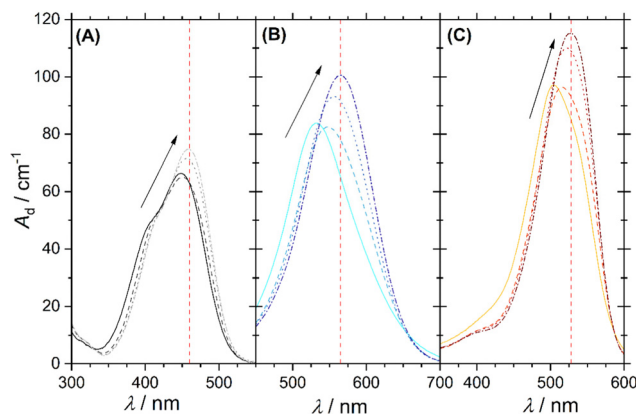
**Fig. 3** Spectra of solutions containing dye (solid line) or dye and DTAB in the homogeneous 1-phase region (dotted/dashed lines). The arrows indicate an increase in DTAB concentration from 0 mM to 90 mM. The red, vertical lines indicate the wavelength at which quantitative analysis was performed. $[Dye]_{tot}$ = 2.5 mM in all cases. (A) Yellow, (B) Blue, (C) Red. At any wavelength, $A_d$ corresponds to the absorbance at that wavelength divided by optical path length $A_d = A/d$ with $d$ = 0.01 cm.

spectrum of the solution of pure dye. The total dye concentration was $[Dye]_{tot}$ = 2.5 mM in all cases. The value $A_d$ designating the $y$-axis of all spectra corresponds to the absorbance $A$ of the sample divided by the optical path length $d$. The optical path length was $d$ = 0.01 cm in all cases. In the present work, $A_d$ was used consistently in place of $A$ in order to simplify calculations and mathematical expressions by not having to consider the path length. $[Dye]_{tot}$ = 2.5 mM was chosen to provide a dye concentration high enough to obtain a reasonable scattering signal during contrast variation SANS experiments, which will be reported more extensively in a follow-up publication. At the same time it is low enough to permit the recording of UV/vis spectra in a cuvette with 0.01 cm path length while not significantly exceeding a maximum absorbance of $A$ = 1.

As visible from Fig. 3, bathochromic shifts of absorption maxima of $\Delta\lambda_{max}$ = 11 nm, $\Delta\lambda_{max}$ = 34 nm and $\Delta\lambda_{max}$ = 24 nm were observed for Yellow, Blue and Red between a solution containing only dye and a solution containing dye and $[DTAB]_{tot}$ = 90 mM. These values signal a bathochromic shift significant enough to perform quantitative evaluation of recorded UV/vis-spectra with respect to an underlying dye–surfactant association equilibrium. For this purpose, dye absorbance was monitored as a function of DTAB concentration at a given wavelength. For Yellow, this wavelength was chosen to $\lambda$ = 460 nm, for Blue to $\lambda$ = 565 nm and for Red to $\lambda$ = 528 nm. These wavelengths are indicated in Fig. 3 by a red, vertical line for each dye. They correspond to the wavelength of maximum absorbance in the sample with highest surfactant excess. $[Dye]_{tot}$ was kept constant at 2.5 mM while varying DTAB concentration between 0 mM < $[DTAB]_{tot}$ < 90 mM.

Fig. 4 shows the development of $A_d$ as a function of $[DTAB]_{tot}$ at $[Dye]_{tot}$ = 2.5 mM for all three dyes at wavelengths indicated in Fig. 3 by the red lines. Fig. 4 permits the distinction of three surfactant concentration regions commonly referred to when observing the aggregation between oppositely charged dye and surfactant:[32,36,39]
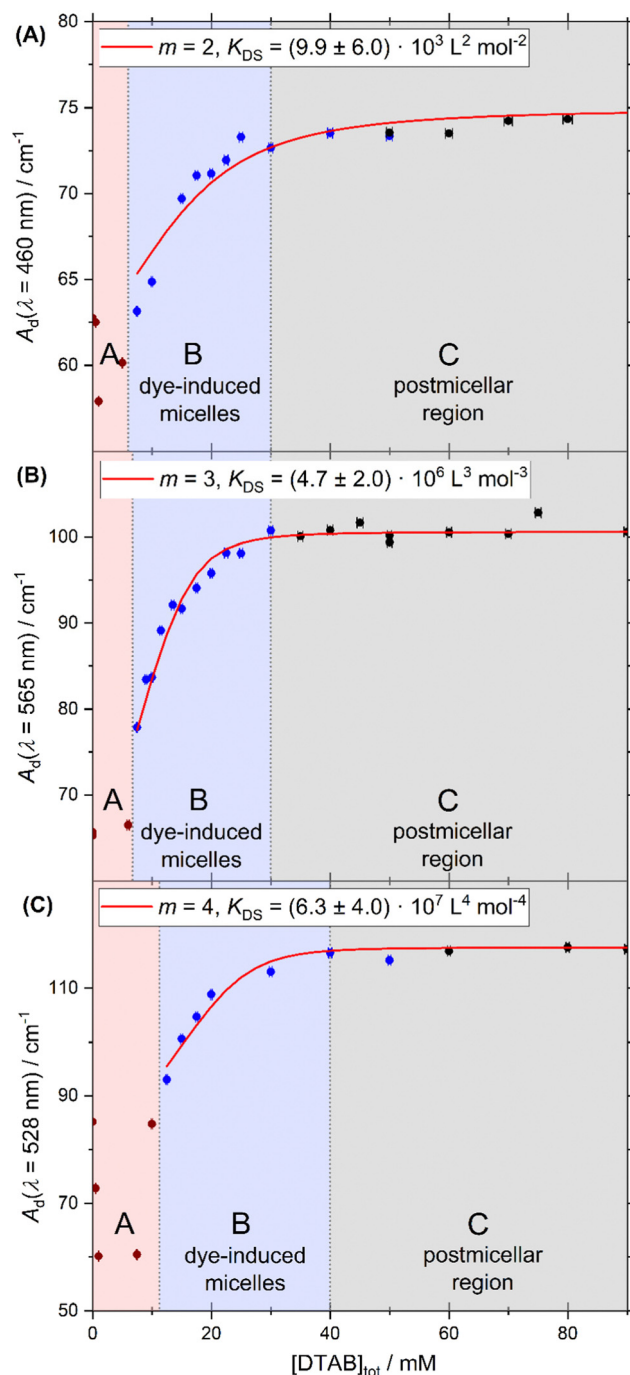


**Fig. 4** Absorption of dye solutions with $[Dye]_{tot}$ = 2.5 mM containing different concentrations of DTAB. Phase-separating samples are indicated by red dots, blue and black dots indicate stable samples in the 1-phase region. Blue data points were used to calculate $K_{DS}$. The red line displays the applied dye–surfactant association model assuming a stoichiometry of $1 : m$ for dye:DTAB binding and the given $K_{DS}$. (A) Yellow, $A_d$ ($\lambda$ = 460 nm), (B) Blue, $A_d$ ($\lambda$ = 565 nm), (C) Red, $A_d$ ($\lambda$ = 528 nm). $A_d$ ($\lambda$ = $x$ nm) corresponds to the absorbance at wavelength $x$ divided by optical path length $A_d = A/d$ with $d$ = 0.01 cm.

**Region A.** Formation of dye–surfactant ion pairs. This corresponds to the 2-phase region in the phase diagrams, where the precipitation of dye–surfactant complexes leads to a strong

decrease in absorbance, as precipitation and filtration of corresponding samples before measurement removes part of the dye.

**Region B.** Dye-induced micelles.[32,39] The region of dye-induced micelles was identified as the DTAB concentration region, where the spectrum of the dye is still sensitive to DTAB concentration changes.[32] Part of it lays below the critical micelle concentration (cmc) of pure DTAB, which was determined to be 9 mM in the present buffer system at 25 °C. In a following paper it will be shown, that micelles are indeed formed in the entire region B.

**Region C.** Postmicellar region. This region is identified by an absence of change in dye absorption upon further addition of DTAB.[32] It lays above DTAB cmc. Ghosh *et al.* referred to the aggregates in this region as dye-embedded micelles.[39] In view of the fact that the dyes and DTAB carry opposite charges, the location of dyes close to the positively charged DTAB head groups is likely. Therefore, the term "dye-embedded micelles" may not be the most accurate description of aggregates in this case. Nevertheless, the excess of surfactant in the post micellar region causes most of the dye molecules to interact with surfactant molecules in corresponding aggregates rather than not interacting with surfactant.

Within the last 70 years, various models were developed for the quantitative evaluation of equilibrium constants from UV/vis-spectroscopic data.[40–42] In the case of solute-surfactant association it is possible to either assume a thermodynamic equilibrium between a solute molecule and $m$ surfactant molecules or between one solute molecule and one surfactant micelle. The latter gives rise to the well-known Benesi–Hildebrand equation frequently used in case of high surfactant excess.[32,34,36,43] In the current system, however, the application of a dye-micelle equilibrium model is not suitable as (1) surfactant concentrations studied are too low to assume surfactant excess and (2) some of the studied surfactant concentrations lay below the cmc of DTAB without the dye. Therefore, an equilibrium between one dye molecule Dye and $m$ free surfactant molecules S on one side and the complex $DyeS_m$ on the other side is considered, assuming that micelle formation does only occur due to the interaction between dye and surfactant.

$$\text{Dye} + m\,\text{S} \rightleftharpoons \text{DyeS}_m \qquad (2)$$

The assumption of a $1:m$ rather than a $1:1$ stoichiometry for dye–surfactant association in solution is reasonable considering observed stoichiometries for dye–surfactant binding determined in eqn (1) for the solid dye–surfactant complex. The equilibrium– or dye–surfactant association constant $K_{DS}$ for eqn (2) can be written as:

$$K_{DS} = \frac{[\text{DyeS}_m]}{[\text{Dye}] \cdot [\text{S}]^m} \qquad (3)$$

$[DyeS_m]$, [Dye] and [S] denote molar equilibrium concentrations of the dye–surfactant complex, dye monomer and surfactant monomer. Our model based on eqn (2) is fully compatible

with the choice of $[\text{Dye}]_{tot} = 2.5$ mM. The model formally describes the co-assembly of one dye molecule with $m$ surfactant molecules in equilibrium with monomeric dye and monomeric surfactant. This feature well includes the possibility of mixed micelles with the same stoichiometry as $DyeS_m$. In other words, if this co-assembly triggers micelle formation it is automatically included.

It is emphasized that preliminary self-assembly equilibria of dye molecules are neglected. Indeed, previous studies on the self-assembly of the three dyes showed, that Blue self-assembles to dimers and Red to fractal-like aggregates, whereas Yellow remains molecularly dissolved in their pure solution without surfactant.[33] However, self-assembly was suggested to be mainly driven by π–π-stacking and hydrogen bonding interactions, which are generally weaker than the strong electrostatic attraction between oppositely charged dye- and surfactant molecules.[26] Therefore, dye–dye complexes are considered to be easily broken apart within dye–DTAB mixed micelles due to strong electrostatic interaction between negatively charged dye molecules and cationic surfactant molecules. An observation confirming preferential binding between dye and DTAB molecules is the precipitation of solid dye–DTAB complexes at small surfactant concentrations (2-phase region, Fig. 2).

Taking total molar concentrations of the dye monomer $[\text{Dye}]_{tot}$ and the surfactant $[\text{S}]_{tot} = [\text{DTAB}]_{tot}$ into account, eqn (3) can be written as:

$$K_{DS} = \frac{[\text{DyeS}_m]}{([\text{Dye}]_{tot} - [\text{DyeS}_m]) \cdot ([\text{S}]_{tot} - m[\text{DyeS}_m])^m} \qquad (4)$$

Assuming that only the dye and the dye–surfactant complex $[DyeS_m]$ absorb at the relevant wavelength (indicated by the red vertical lines of Fig. 3) and assuming the validity of Beer–Lambert Law for both species, the absorbance of a sample can be expressed as:

$$A_d = \varepsilon_{\text{Dye}} \cdot [\text{Dye}] + \varepsilon_{\text{DS}_m} \cdot [\text{DyeS}_m] \qquad (5)$$

With $[\text{Dye}] = [\text{Dye}]_{tot} - [\text{DyeS}_m]$ and with $A_{d,0} = \varepsilon_{\text{Dye}}[\text{Dye}]_{tot}$, eqn (6) as an expression for $[DyeS_m]$ is revealed:

$$[\text{DyeS}_m] = \frac{A_d - A_{d,0}}{\varepsilon_{\text{DS}_m} - \varepsilon_{\text{Dye}}} \qquad (6)$$

$\varepsilon_{\text{Dye}}$ and $\varepsilon_{\text{DS}_m}$ are the molar extinction coefficients of the dye and the dye–surfactant complex respectively. Assuming a stoichiometry $m$, a value $K_{DS}$ can therefore be calculated from each data pair $A_d = f([\text{S}]_{tot})$ by substituting eqn (6) into eqn (4). $A_{d,0}$ and $\varepsilon_{\text{Dye}}$ are known from the absorption spectrum of pure dye, whereas $\varepsilon_{\text{DS}}$ was obtained from the sample with maximum surfactant excess, located in the postmicellar region where dye absorption does not change upon further addition of surfactant.

Model fits were carried out with six stoichiometries. For a given stoichiometry $m$, $K_{DS}$ was determined from the $A_d = f([\text{S}]_{tot})$ data pair of $N$ samples mostly located in the region of dye-induced micelles and indicated as blue data points in Fig. 4. The average of all $K_{DS}$ obtained for this stoichiometry

$m$ was then taken and used to calculate the theoretical absorbance $A_{d,theo}$ for each of the $N$ samples. The deviation of $A_{d,theo}$ from the recorded absorbance $A_d$ of the respective sample yielded the $\chi_{red}^2$ value defined by eqn (7).

$$\chi_{red}^2 = \frac{\sum_{i=1}^{N}\left(A_{d,i} - A_{d,theo,i}\right)^2}{N} \qquad (7)$$

This procedure was performed for six stoichiometries. Corresponding $\chi_{red}^2$ values are reported in Table 1 for each dye. Due to the absence of specific spectral features signalling a build-up and disassembly or modification of soluble dye–surfactant complexes $DyeS_m$ at a $1:m$ ratio, it was not possible to employ a more straightforward analysis technique to obtain information on the stoichiometry of dye–surfactant binding.[44] Furthermore, as discussed earlier, the application of a previously reported analysis technique assuming $1:1$ stoichiometry of dye–surfactant binding in the region of dye-induced micelles (B, Fig. 4) would have been unreasonable.[45] Therefore, strategy to obtain information on stoichiometry $m$ and association $K_{DS}$ of dye–surfactant binding, presented here, is considered to be most suitable for the system under consideration.

The data are best described by a stoichiometry $m$ at which the lowest $\chi_{red}^2$ is obtained. This stoichiometry, together with the corresponding dye–surfactant association constant $K_{DS}$ is summarized in Table 2. $A_{d,theo} = f([S]_{tot})$ based on these values is displayed in Fig. 4 as a red curve. Experimental data points are reasonably well described by these curves so that the model can be considered to be a relatively good approximation under the given conditions.

Association constants $K_{DS}$ obtained by this procedure suffer from considerable uncertainties. However, information about their order of magnitude is obtained. In addition to that, all $K_{DS}$ lay well above 1, which means that dye–surfactant complex formation is strongly favoured.

It is remarkable that the stoichiometry of dye : DTAB binding decreases from $1:2$ for Yellow over $1:3$ for Blue to $1:4$ for Red. The same trend was established for the stoichiometry of dye : DTAB binding from evaluation of the phase transition threshold line in the phase diagrams (Fig. 2). In addition to that, the number of DTAB molecules aggregating with one dye molecule in the homogeneous 1-phase region is always higher than that obtained from the analysis of the phase transition threshold in the phase diagram. This is consistent with the assumption that soluble $DyeS_m$ aggregates are only formed below a certain dye : DTAB threshold ratio.
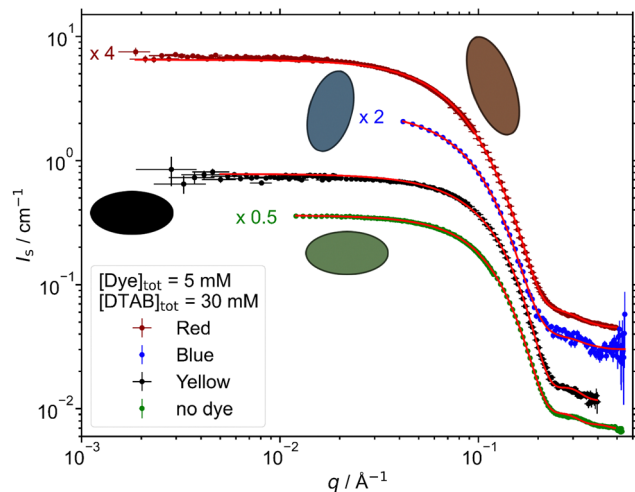
### Small-angle neutron scattering

SANS studies were performed on samples which, according to their dye : DTAB ratio, lay within the region of dye-induced micelles. The impact of adding different dye molecules at a concentration of $[Dye]_{tot} = 5$ mM on the morphology of DTAB micelles was studied. Fig. 5 displays SANS curves from solutions containing $[Dye]_{tot} = 5$ mM and $[DTAB]_{tot} = 30$ mM in comparison to the SANS curve of pure DTAB at that concentration. The latter was described with the form factor model of an oblate ellipsoid including a structure factor derived by Hayter and Penfold to consider inter-micellar interaction.[46,47] The choice of this model was based on work by Bergström and Pedersen whom investigated the morphology of DTAB micelles in brine solution.[48] The use of such a structure factor significantly improved quality of the fit, even though no obvious correlation peak is visible in the dilute solution of DTAB (Fig. 5), which also contains a rather high concentration of buffer salt (ionic strength $I \approx 0.25$ M).

For the description of SANS curves originating from solutions containing both, dye and DTAB, no structure factor was used, as the anionic dye is assumed to interact with the positively charged DTAB head group, which leads to charge screening and reduces medium- to long-range ordering caused by electrostatic interactions.[49] The SANS curve of Yellow was well described using the form factor of an oblate ellipsoid with dimensions similar to the pure DTAB micelle (Table 3).

For the description of SANS curves emerging from solutions of Blue with DTAB and Red with DTAB, the assumption of a more anisometric micellar morphology became necessary. This was realized by moving to a triaxial ellipsoid model to fit the data.[50] Resulting geometrical dimensions are displayed in Table 3. Interestingly, the two smaller radii of each triaxial ellipsoid are similar to the polar and equatorial radius $r_p$ and $r_{eq}$ of oblate ellipsoidal DTAB micelles. This points towards an one-dimensional growth of DTAB micelles upon addition of dye, like it is frequently observed for cationic surfactant micelles upon addition of salt or hydrotrope.[51–53]

**Table 1** Evaluation of the stoichiometry of the dye−surfactant association equilibrium with $\chi_{red}^2$ defined by eqn (7) as criterium

| Dye | Yellow | Blue | Red |
|---|---|---|---|
| Data interval | $7.5$ mM $\leq$ $[S]_{tot} \leq 50$ mM | $7.5$ mM $\leq$ $[S]_{tot} \leq 25$ mM | $12.5$ mM $\leq$ $[S]_{tot} \leq 55$ mM |
| $m$ | $\chi_{red}^2$ | $\chi_{red}^2$ | $\chi_{red}^2$ |
| 1 | 29.78 | 145.97 | 44.53 |
| 2 | **1.64** | 137.88 | 11.26 |
| 3 | 51.28 | **2.22** | 4.64 |
| 4 | 66.02 | 378.88 | **3.35** |
| 5 | 71.83 | 626.11 | 4.02 |
| 6 | 74.03 | 608.56 | 5.19 |

**Table 2** Stoichiometry and association constants for the association equilibrium of dye−surfactant complexes

| Dye | Yellow | Blue | Red |
|---|---|---|---|
| $m$ | 2 | 3 | 4 |
| $K_{DS}(m)$ $[L^m\ mol^{-m}]$ | $(9.9 \pm 6.0) \times 10^3$ | $(4.7 \pm 2.0) \times 10^6$ | $(6.3 \pm 4.0) \times 10^7$ |
| $\chi_{red}^2$ | 1.64 | 2.22 | 3.35 |

**Fig. 5** SANS curves of solutions containing [Dye]$_{tot}$ = 5 mM and [DTAB]$_{tot}$ = 30 mM and a solution containing DTAB at a concentration of 30 mM without dye. Samples were prepared in a NaHCO$_3$/Na$_2$CO$_3$ buffer (pD = 10.7, $I \approx$ 0.25 M) in D$_2$O except for the sample containing Blue, where the buffer was dissolved in a mixture of H$_2$O and D$_2$O (50 : 50, v/v). Fits are shown as red lines. The form factor models are sketched next to the corresponding curve.
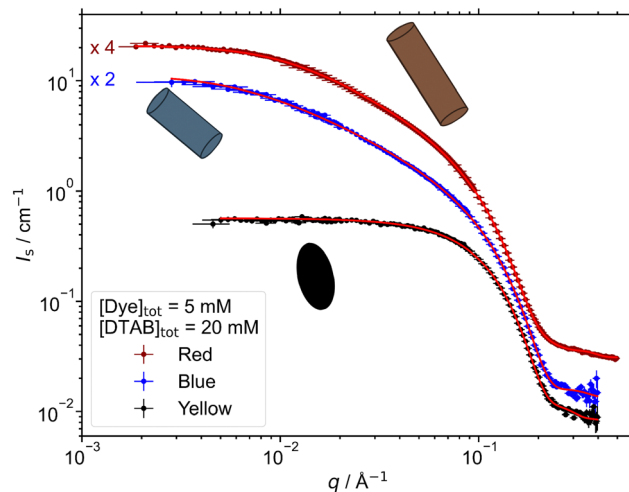


**Fig. 6** SANS curves of solutions containing [Dye]$_{tot}$ = 5 mM and [DTAB]$_{tot}$ = 20 mM. Samples were prepared in an NaHCO$_3$/Na$_2$CO$_3$ buffer (pD = 10.7, $I \approx$ 0.25 M) in D$_2$O. Fits are shown as red lines. The form factor models are sketched next to the corresponding curve.

Moving on to a DTAB concentration of [DTAB]$_{tot}$ = 20 mM while remaining at [Dye]$_{tot}$ = 5 mM, micelle morphologies were found to become more anisometric compared to [DTAB]$_{tot}$ = 30 mM (Fig. 6). This is in agreement with literature. A decrease in the spontaneous curvature of surfactant micelles was frequently observed upon hydrotrope addition.[53–55] This was also the case for the addition of dye molecules to surfactant systems, with the morphology of assemblies depending on the system in use.[56–58]

In the present work, the SANS curve from a solution of Yellow and DTAB was described with the form factor model of a triaxial ellipsoid, whereas SANS curves from solutions of Blue or Red and DTAB were described with the form factor model of a cylinder with elliptical cross section.[46] The corresponding fit parameters can be found in Table 4. Micelles of Blue or Red and DTAB are very polydisperse in length, which makes sense considering the underlying dynamic equilibrium present

in micellar surfactant solutions.[59] To fit the data, the ratio between the root-mean-square deviation from the average length ($\sigma$) and the average length ($L_{avg}$) was set to $\sigma/L_{avg}$ = 0.95 for Blue–DTAB micelles according to a strategy employed by Bergström and Pedersen who observed polydisperse mixed micelles formed from sodiumdodecylsulphate and DTAB.[60] It was intended to use the same $\sigma/L_{avg}$ for the SANS curve emerging from the corresponding Red–DTAB solution. However, the data was better described using $\sigma/L_{avg}$ = 0.5. Strikingly, the dimensions of the elliptical cylinder cross section remain very similar to $r_{eq}$ and $r_p$ found for DTAB micelles at [DTAB]$_{tot}$ = 30 mM (Table 4). This confirms the assumption of an unidimensional growth of these micelles upon increase of the dye : DTAB ratio from 1 : 6 to 1 : 4.

The differences in the morphologies of dye–DTAB micelles observed for the different dyes correlate with the stoichiometries found for dye–DTAB binding from the phase transition threshold as well as in solution. This can easily be related to the SANS sample composition relative to the phase transition threshold in the concentration-dependent phase diagrams of

**Table 3** Model parameters from form factor fits to SANS curves resulting from solutions containing dye at a concentration of [Dye]$_{tot}$ = 5 mM and DTAB at a concentration of [DTAB]$_{tot}$ = 30 mM. Samples were prepared in an aqueous NaHCO$_3$/Na$_2$CO$_3$ buffer (pD = 10.7, $I \approx$ 0.25 M) in D$_2$O except for the sample containing Blue where the buffer was prepared in a H$_2$O/D$_2$O mixture (50 : 50 v/v) as described in the experimental part. For fitting the SANS curve emerging from a pure DTAB solution, the product of an oblate ellipsoidal form factor and a structure factor by Hayter and Penfold was used.[46,47] In the case of the form factor model of a triaxial ellipsoid, the length parameter is equivalent to the longest radius

| | | Cross section | | Length |
|---|---|---|---|---|
| Dye | Model | $r_{minor}$/Å | $r_{major}$/Å | $L$/Å |
| No dye | Oblate ellipsoid[a] | $r_{eq}$ = 22.357 ± 0.009 | | $r_p$ = 14.048 ± 0.008 |
| Yellow | Oblate ellipsoid | $r_{eq}$ = 21.73 ± 0.04 | | $r_p$ = 13.98 ± 0.06 |
| Blue | Triaxial ellipsoid | 15.3 ± 0.2 | 22.0 ± 0.3 | 32.0 ± 0.3 |
| Red | Triaxial ellipsoid | 15.93 ± 0.02 | 22.32 ± 0.03 | 40.31 ± 0.04 |

[a] Oblate ellipsoid × structure factor; symbols: $r_p$ – polar radius, $r_{eq}$ – equatorial radius, $r_{minor}$ – minor cross section radius, $r_{major}$ – major cross section radius, $L$ – length.

**Table 4** Model parameters from form factor fits to SANS curves resulting from solutions containing dye at a concentration of $[Dye]_{tot}$ = 5 mM and DTAB at a concentration of $[DTAB]_{tot}$ = 20 mM. Samples were prepared in an aqueous $NaHCO_3/Na_2CO_3$ buffer (pD = 10.7, $I \approx 0.25$ M) in $D_2O$. In the case of the form factor model of a triaxial ellipsoid, the length parameter is equivalent to the longest radius

| Dye | Model | Cross Section | | Length |
| --- | --- | --- | --- | --- |
| | | $r_{minor}/Å$ | $r_{major}/Å$ | $L/Å$ |
| Yellow | Triaxial ellipsoid | $13.8 \pm 0.2$ | $21.6 \pm 0.6$ | $24.4 \pm 0.6$ |
| Blue | Cylinder with elliptical cross section | $13.1 \pm 0.2$ | $19.6 \pm 0.4$ | $L = 199 \pm 3$ $\sigma/L_{avg} = 0.95$ |
| Red | Cylinder with elliptical cross section | $14.19 \pm 0.02$ | $23.64 \pm 0.05$ | $L = 233.5 \pm 0.7$ $\sigma/L_{avg} = 0.5$ |

Symbols: $\sigma/L_{avg}$ – ratio of the root-mean-square deviation from the average length and the average length.

Fig. 2. For the dye Red, the sample compositions investigated with SANS, *i.e.* $[Dye]_{tot}$ = 5 mM and $[DTAB]_{tot}$ = 20 mM or 30 mM lay much closer to its phase transition threshold than for Blue or Yellow. Conversely, the phase transition threshold in the phase diagram of Yellow and DTAB is the farthest away from these sample compositions. The micelles formed between $[Yellow]_{tot}$ = 5 mM and $[DTAB]_{tot}$ = 30 mM are about the same size as pure DTAB micelles, indicating that the composition of this sample presumably lays close to the post-micellar region, where assembly morphology is determined by DTAB micelles due to their excess presence. Furthermore, it is logical to assume a DTAB excess at a Yellow : DTAB ratio of 1 : 6, considering that Yellow and DTAB interact at a stoichiometry of 1 : 2 (Table 2).

To conclude, the morphology of dye–surfactant micelles depends on the dye added to the solution. The magnitude of observed deviations from the morphology of pure DTAB micelles at a given sample composition inversely correlates with dye : DTAB binding stoichiometries found at the phase transition threshold as well as in solution. The one-dimensional growth of DTAB micelles upon dye addition was strongest for the addition of Red, which binds to DTAB at a stoichiometry of Red : DTAB = 1 : 4 in solution, medium for the addition of Blue with a stoichiometry of Blue : DTAB = 1 : 3 and weakest for Yellow with a stoichiometry of Yellow : DTAB = 1 : 2. A general increase in micellar anisometry when increasing the dye : DTAB ratio from 1 : 6 to 1 : 4, *i.e.* when moving closer to the phase transition threshold from the side of DTAB excess, was observed for all dyes.

## Conclusions

Three 3-chloro-4-hydroxy-phenylazo dyes, each of them carrying a negative charge due to deprotonation of the phenolic hydroxyl group at alkaline pH, were shown to differ in the stoichiometry of their co-assembly with the cationic surfactant DTAB.

For all dyes, phase separation of dye–DTAB solutions was observed above a given dye : DTAB ratio with the ratio depending on the dye. It was observed to decrease from Yellow (1 : 1.67) over Blue (1 : 2.56) to Red (1 : 2.94) and gives an indication of the stoichiometry of dye–DTAB binding in the coacervate phase for Yellow or the solid precipitate for Blue and Red.

Furthermore, the stoichiometry of dye–DTAB binding in solution, *i.e.* the 1-phase region, was studied using UV/vis

spectroscopy. Stoichiometries of 1 : 2, 1 : 3 and 1 : 4 were found for Yellow, Blue and Red with DTAB respectively. The lower dye : DTAB ratios obtained in homogeneous solution as compared to the ratios at the respective phase transition threshold can nicely be reconciled with a larger amount of DTAB molecules required for the solubilisation of dye compared to that of the formation of solid complexes.

Furthermore, the morphology of dye–DTAB micelles was studied using SANS. DTAB micelles show an uniaxial growth upon dye addition with its extend being dependent upon the dye and being inversely correlated to dye : DTAB binding stoichiometry at a set total concentration of dye and DTAB. This was attributed to a sample composition being closer to the postmicellar region if the dye : DTAB binding stoichiometry is high, *e.g.* Yellow : DTAB = 1 : 2, or closer to the phase transition threshold or region of dye–surfactant ion pair formation for a low binding stoichiometry, *e.g.* Red : DTAB = 1 : 4. A sample being close to the postmicellar region indicates surfactant excess, which leads to micellar morphology being largely determined by the morphology of surfactant micelles.

Following the presented investigations, differences in the co-assembly behaviour of three structurally similar azo dyes with DTAB were elucidated. Differences in co-assembly morphology were related to the stoichiometry of dye–DTAB binding. It becomes clear, that even structurally similar molecules can show significant differences in their interaction with a surfactant.

## Author contributions

Conceptualization: WM, RS, BN, KH, experimental: WM, RS, GS, JK, analysis: WM with contributions from RS, GS, KH, BN, writing: WM, editing: RS, BN, KH, GS, funding acquisition: RS, BN, KH

## Conflicts of interest

There are no conflicts to declare.

## Acknowledgements

## Notes and references

1 G. A. Silva, C. Czeisler, K. L. Niece, E. Beniash, D. A. Harrington, J. A. Kessler and S. I. Stupp, *Science*, 2004, **303**, 1352–1355.

2 K. Rajangam, H. A. Behanna, M. J. Hui, X. Han, J. F. Hulvat, J. W. Lomasney and S. I. Stupp, *Nano Lett.*, 2006, **6**, 2086–2090.

3 S. Zhou, C. Burger, B. Chu, M. Sawamura, N. Nagahama, M. Toganoh, U. E. Hackler, H. Isobe and E. Nakamura, *Science*, 2001, **291**, 1944–1947.

4 D. E. Discher and A. Eisenberg, *Science*, 2002, **297**, 967–973.

5 A. P. H. J. Schenning, J. v Herrikhuyzen, P. Jonkheijm, Z. Chen, F. Würthner and E. W. Meijer, *J. Am. Chem. Soc.*, 2002, **124**, 10252–10253.

6 A. N. Shipway, E. Katz and I. Willner, *ChemPhysChem*, 2000, **1**, 18–52.

7 O. D. Velev and E. W. Kaler, *Langmuir*, 1999, **15**, 3693–3698.

8 D. J. Norris and Yu. A. Vlasov, *Adv. Mater.*, 2001, **13**, 371–376.

9 O. D. Velev and E. W. Kaler, *Adv. Mater.*, 2000, **12**, 531–534.

10 L. C. Palmer, Y. S. Velichko, M. Olvera de la Cruz and S. I. Stupp, *Philos. Trans. R. Soc., A*, 2007, **365**, 1417–1433.

11 M. Rubinstein and G. A. Papoian, *Soft Matter*, 2012, **8**, 9265–9267.

12 H. J. Kwon and J. P. Gong, *Curr. Opin. Colloid Interface Sci.*, 2006, **11**, 345–350.

13 G. Du, D. Belić, A. Del Giudice, V. Alfredsson, A. M. Carnerup, K. Zhu, B. Nyström, Y. Wang, L. Galantini and K. Schillén, *Angew. Chem.*, 2022, **134**, e202113279.

14 N. Carl, S. Prévost, R. Schweins and K. Huber, *Soft Matter*, 2019, **15**, 8266–8271.

15 M. Antonietti, J. Conrad and A. Thuenemann, *Macromolecules*, 1994, **27**, 6007–6011.

16 S. G. Trindade, L. Piculell and W. Loh, *Langmuir*, 2022, **38**, 2906–2918.

17 I. Willerich and F. Gröhn, *Angew. Chem., Int. Ed.*, 2010, **49**, 8104–8108.

18 N. Carl, W. Müller, R. Schweins and K. Huber, *Langmuir*, 2020, **36**, 223–231.

19 A. Zika, M. Agarwal, R. Schweins and F. Gröhn, *Chem. – Eur. J.*, 2022, **29**, e202203373.

20 I. Willerich and F. Gröhn, *J. Am. Chem. Soc.*, 2011, **133**, 20341–20356.

21 S. Kanai and M. Muthukumar, *J. Chem. Phys.*, 2007, **127**, 244908.

22 H. M. Fares and J. B. Schlenoff, *J. Am. Chem. Soc.*, 2017, **139**, 14656–14667.

23 K. Kolman, G. Poggi, M. Baglioni, D. Chelazzi, P. Baglioni, M. Persson, K. Holmberg and R. Bordes, *J. Colloid Interface Sci.*, 2022, **615**, 265–272.

24 Y. Guan, M. Antonietti and C. F. J. Faul, *Langmuir*, 2002, **18**, 5939–5945.

25 C. F. J. Faul and M. Antonietti, *Chem. – Eur. J.*, 2002, **8**, 2764–2768.

26 C. F. J. Faul and M. Antonietti, *Adv. Mater.*, 2003, **15**, 673–683.

27 Mantid Project, Mantid (2013): Manipulation and Analysis Toolkit for Instrument Data, DOI: **10.5286/SOFTWARE/ MANTID**.

28 O. Arnold, J. C. Bilheux, J. M. Borreguero, A. Buts, S. I. Campbell, L. Chapon, M. Doucet, N. Draper, R. Ferraz Leal, M. A. Gigg, V. E. Lynch, A. Markvardsen, D. J. Mikkelson, R. L. Mikkelson, R. Miller, K. Palmen, P. Parker, G. Passos, T. G. Perring, P. F. Peterson, S. Ren, M. A. Reuter, A. T. Savici, J. W. Taylor, R. J. Taylor, R. Tolchenov, W. Zhou and J. Zikovsky, *Nucl. Instrum. Methods Phys. Res., Sect. A*, 2014, **764**, 156–166.

29 *Neutrons, X-rays, and light: scattering methods applied to soft condensed matter*, ed. P. Lindner and T. Zemb, Elsevier, Amsterdam, Boston, 1st edn, 2002.

30 U. Keiderling, *Appl. Phys. A: Mater. Sci. Process.*, 2002, **74**, s1455–s1457.

31 G. K. G. Carvalho Barros, L. J. N. Duarte, R. P. F. Melo, F. W. B. Lopes and E. L. Barros Neto, *J. Polym. Environ.*, 2022, **30**, 2534–2546.

32 O. Owoyomi, O. Z. Junaid and O. E. Olaoye, *Phys. Chem. Liq.*, 2021, **60**, 129–140.

33 W. Müller, R. Schweins, B. Nöcker, H. Egold and K. Huber, *Soft Matter*, 2023, DOI: **10.1039/d3sm00500c**.

34 R. Sabaté, M. Gallardo, A. de la Maza and J. Estelrich, *Langmuir*, 2001, **17**, 6433–6437.

35 S. S. Shah, S. W. H. Shah and K. Naeem, *Encyclopedia of Surface and Colloid Science*, Taylor & Francis, 3rd edn, 2015, pp. 7141–7149.

36 P. Shah, S. Kumari Jha and A. Bhattarai, *J. Mol. Liq.*, 2021, **340**, 117200.

37 R. K. Dutta and S. N. Bhat, *Can. J. Chem.*, 1993, **71**, 1785–1791.

38 A. Rehman, M. U. Nisa, M. Usman, Z. Ahmad, T. H. Bokhari, H. M. A. U. Rahman, A. Rasheed and L. Kiran, *J. Mol. Liq.*, 2021, 115345.

39 D. C. Ghosh, P. K. Sen and B. Pal, *Int. J. Chem. Kinet.*, 2021, **53**, 1228–1238.

40 N. J. Rose and R. S. Drago, *J. Am. Chem. Soc.*, 1959, **81**, 6138–6141.

41  B. K. Seal, A. K. Mukherjee and D. C. Mukherjee, *BCSJ*, 1979, **52**, 2088–2090.

42  H. A. Benesi and J. H. Hildebrand, *J. Am. Chem. Soc.*, 1949, **71**, 2703–2707.

43  J. R. Perussi, V. E. Yushmanov, S. C. Monte, H. Imasato and M. Tabak, *Physiol. Chem. Phys. Med. NMR*, 1995, **27**, 1–15.

44  K. K. Karukstis, D. A. Savin, C. T. Loftus and N. D. D'Angelo, *J. Colloid Interface Sci.*, 1998, **203**, 157–163.

45  M. Bielska, A. Sobczyńska and K. Prochaska, *Dyes Pigm.*, 2009, **80**, 201–205.

46  L. A. Feigin and D. I. Svergun, *Structure Analysis by Small-Angle X-Ray and Neutron Scattering*, Springer, US, 1987.

47  J. B. Hayter and J. Penfold, *Mol. Phys.*, 1981, **42**, 109–118.

48  M. Bergstrom and J. Pedersen, *Phys. Chem. Chem. Phys.*, 1999, **1**, 4437–4446.

49  P. A. Hassan, G. Fritz and E. W. Kaler, *J. Colloid Interface Sci.*, 2003, **257**, 154–162.

50  J. A. Finnigan and D. J. Jacobs, *J. Phys. D: Appl. Phys.*, 1971, **4**, 72.

51  C. A. Dreiss, *Soft Matter*, 2007, **3**, 956–970.

52  F. Quirion and L. J. Magid, *J. Phys. Chem.*, 1986, **90**, 5435–5441.

53  N. Onoda-Yamamuro, O. Yamamuro, N. Tanaka and H. Nomura, *J. Mol. Liq.*, 2005, **117**, 139–145.

54  C. A. Dreiss, *Wormlike Micelles: Advances in Systems, Characterisation and Applications*, Royal Society of Chemistry, 2017, pp. 1–8.

55  E. J. Creatto, F. B. Okasaki, M. B. Cardoso and E. Sabadini, *J. Colloid Interface Sci.*, 2022, **627**, 355–366.

56  D. Wang, P. Long, R. Dong and J. Hao, *Langmuir*, 2012, **28**, 14155–14163.

57  L. Li, Y. Yang, J. Dong and X. Li, *J. Colloid Interface Sci.*, 2010, **343**, 504–509.

58  A. Kutz, G. Mariani and F. Gröhn, *Colloid Polym. Sci.*, 2016, **294**, 591–606.

59  A. Patist, S. G. Oh, R. Leung and D. O. Shah, *Colloids Surf., A*, 2001, **176**, 3–16.

60  M. Bergström and J. S. Pedersen, *Langmuir*, 1999, **15**, 2250–2253.